

Article

Stepwise Removal Process Analysis Based on Layered Corrosion Oxides

Yuan Ren ^{1,2,3}, Liming Wang ^{1,2,*} , Mingliang Ma ^{1,2}, Wei Cheng ^{3,4}, Baoli Li ⁵, Yuxin Lou ⁴, Jianfeng Li ^{1,2,*} and Xinqiang Ma ^{2,3,4,*}

- ¹ Key Laboratory of High Efficiency and Clean Mechanical Manufacture, Ministry of Education, School of Mechanical Engineering, Shandong University, Jinan 250061, China
² National Demonstration Center for Experimental Mechanical Engineering Education, Shandong University, Jinan 250061, China
³ Laser Institute, Qilu University of Technology (Shandong Academy of Sciences), 3501 Daxue Road, Jinan 250100, China
⁴ Shandong Qiangyuan Laser of Sdiit Ltd., Liaocheng 252022, China
⁵ Liaocheng Institutes of Industrial Technology, Liaocheng 252002, China
* Correspondence: liming_wang@sdu.edu.cn (L.W.); ljf@sdu.edu.cn (J.L.); maxinqiang@sdlaser.cn (X.M.)

Abstract: The parts of engineering machinery quickly generate rusty oxides in the working process, which seriously affects their service life and safety. How to remove oxides efficiently without damaging the surface of the matrix is a crucial problem. This paper analyzes the critical laser parameters that affect the distribution of material temperature field, which determines the ablation depth of different oxides, by using the central composite experimental design method and taking the surface-ablation depth of Fe₂O₃ and Fe₃O₄ before and after laser cleaning as response variables to establish the prediction model of single removal volume with the help of Comsol Multiphysics software. The results show a positive correlation between ablation depth and peak power density and a negative correlation with scanning speed. In this process, the experimental results show that the prediction model is natural and effective. A flow chart of laser stepwise cleaning of layered corroded oxides can provide theoretical guidance for the laser cleaning of engineering machinery.

Keywords: engineering machinery; laser cleaning; central composite experimental test; ablation depth; prediction model



Citation: Ren, Y.; Wang, L.; Ma, M.; Cheng, W.; Li, B.; Lou, Y.; Li, J.; Ma, X. Stepwise Removal Process Analysis Based on Layered Corrosion Oxides. *Materials* **2022**, *15*, 7559. <https://doi.org/10.3390/ma15217559>

Academic Editor: Amir Mostafaei

Received: 23 September 2022

Accepted: 25 October 2022

Published: 27 October 2022

Publisher's Note: MDPI stays neutral with regard to jurisdictional claims in published maps and institutional affiliations.



Copyright: © 2022 by the authors. Licensee MDPI, Basel, Switzerland. This article is an open access article distributed under the terms and conditions of the Creative Commons Attribution (CC BY) license (<https://creativecommons.org/licenses/by/4.0/>).

1. Introduction

As an essential material in the industry, steel has massive output and demand every year. Q345 steel is widely used in the industrial field given its good strength, electrical conductivity, and all-around performance, especially in engineering machinery [1,2]. However, the working environment is harsh, and the iron matrix is prone to reacting electrochemically with oxygen and water to form rusty oxides. Rusty oxides seriously affect the performance and safety coefficient of parts. The direct loss caused by corrosion is up to hundreds of millions of USD annually [3]. Traditional dedusting technologies include chemical cleaning, high-pressure water-jet cleaning, shot-blasting cleaning, etc. Due to environmental pollution, the rust-returning phenomenon, and operation difficulty, they do not conform to the development path of green cleaning [4–6]. As an emerging cleaning technology, considering its advantages of non-contact cleaning, green cleaning, and good controllability, laser-cleaning technology is gradually replacing traditional cleaning technology and is being applied in the industrial field.

Laser-cleaning technology is based on physical–chemical reactions between laser and pollutions, which can remove the attachment from the material surface through ablation, thermal-stress vibration, and the plasma effect [7,8]. Regarding the effective removal of rusty oxides on the surface of materials, scholars have conducted a certain degree of

research in the past few decades. For laser cleaning for rusty oxides, Ristic used an Nd:YAG pulsed laser to clean corrosion on the metal surface. It was found that the laser energy density was the critical parameter that affected the cleaning quality, and an energy density that was too small and high would cause poor cleaning quality [9]. Osticioli analyzed the chemical-reaction process between the dirt components in the laser-cleaning process under different pulse widths and found that compared with a long pulse, the short-pulse laser could remove surface rust without damaging the substrate [10]. Ali compared the effects of 1064 nm and 532 nm lasers on the surface-corrosion removal of low-carbon steel. The results showed that a 1064 nm wavelength laser was more suitable for cleaning the oxide between the cleaning and damage threshold. In this process, the surface roughness and microhardness of the sample were improved after cleaning [11]. Xu investigated the influence law between cleaning effect and laser power, scanning speed, repetition rate, and pulse duration, and the optimized parameters were obtained. Meanwhile, the heat and thermal-stress equations were used to simulate the cleaning effect with the influence of these parameters, which was in good agreement with the experimental data [12]. Scholars used simulated measures to further explore laser cleaning on different materials. Based on Ansys software, Yue investigated the effects of other temporal pulses on micro-tapered slots covered by an oil film, which laid down a theoretical base for actual cleaning work [13]. Lu successfully established a theoretical model of nanosecond laser peeling off the paint. This model could predict the academic cleaning and damage thresholds based on the mechanism of thermal stress [14]. Marimuthu used a two-dimensional transient numerical simulation to study the material-ablation characteristics and substrate thermal effects in laser cleaning of aerospace alloys. In this process, the mechanism of the excimer laser cleaning was proposed [15].

The working environment of mechanical engineering is harsh, and the surface dirt composition of the parts is more complex. A fundamental problem is how to effectively remove rusty oxide without damaging the surface of the matrix. This paper establishes a layered model of laser cleaning based on the attachment composition of the Q345 steel surface. The central composite test was designed to show the single-pulse-removal volume-prediction model of layered materials with the help of Comsol Multiphysics software, which provides theoretical and technical guidance for practical industrial cleaning.

2. Layered Model and Numerical Simulation

2.1. Simulation Preparation

The oxide layer (Fe_3O_4) and the rust layer (Fe_2O_3) on the surface of Q345 carbon steel were cleaned by a laser as the research object of the simulation, and the laser-cleaning light source simulated the pulsed-fiber-laser cleaning equipment (QYCL-FP200, Shandong Qiangyuan Laser of Sdiit Ltd., Liaocheng, China). The pulse frequency is adjustable from 10 to 1000 kHz and the pulse width is adjustable from 50 to 500 ns. The spot diameter was set as 0.5 mm, the peak power density of the laser is proportional to the average power of the laser, and the laser-energy density can be changed by controlling the average power of the laser. Based on scanning-electron-microscope and X-ray-diffraction analysis, the attachment composition on the Q345 matrix was determined to be the layered structure of Fe_2O_3 and Fe_3O_4 , as shown in Figures 1 and 2.

2.2. Numerical Simulation

Lasers and their materials have three heat processes: conduction, convection, and radiation [16]. Considering the short pulse duration and high peak power for nanosecond lasers, the heat convection and radiation can be neglected in the layered model; heat conduction is the only formation used in Comsol Multiphysics software 6.0.

Comsol Multiphysics software 6.0 was used to draw a two-dimensional layered model, as shown in Figure 3, and the properties of each layer of material are shown in Table 1. The model is divided by local mesh refinement; the model's surface area with direct laser action is densely gridded, and the grid far from the laser-action area is of average size. This

division method can ensure the accuracy of calculation results and improve the computer's running speed.

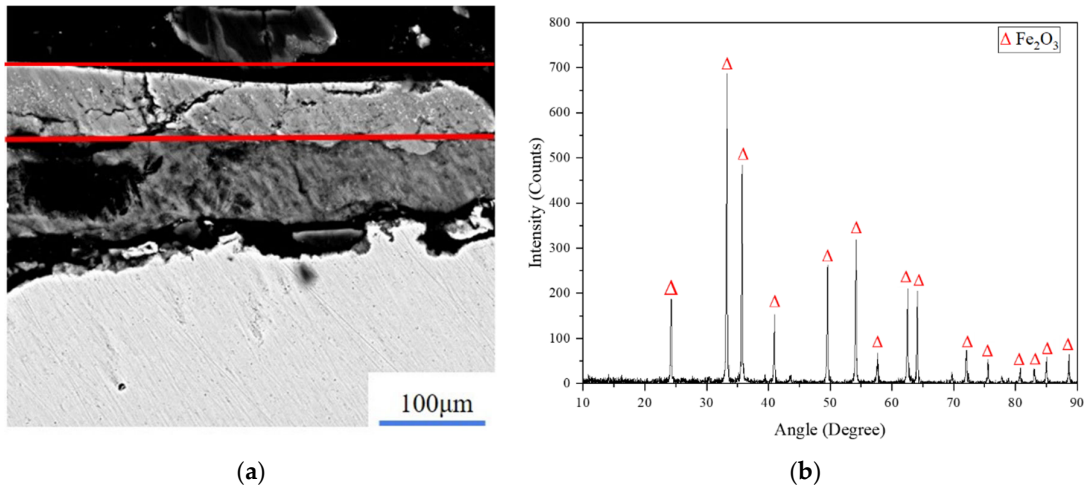


Figure 1. The layered structure distribution of Fe₂O₃ and X-ray-diffraction analysis. (a) Distribution of Fe₂O₃; (b) X-ray-diffraction analysis of Fe₂O₃.

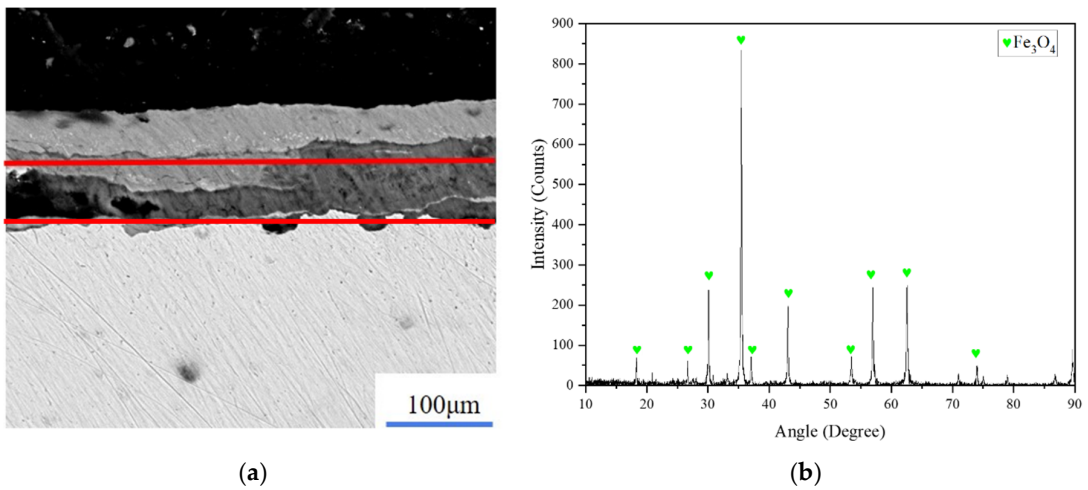


Figure 2. The layered structure distribution of Fe₃O₄ and X-ray-diffraction analysis. (a) Distribution of Fe₃O₄; (b) X-ray-diffraction analysis of Fe₃O₄.

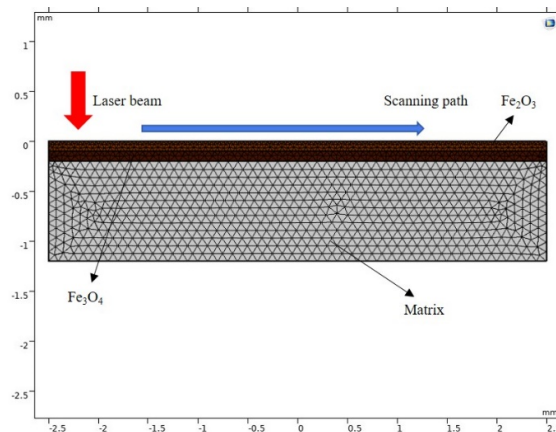


Figure 3. Layered model of cleaning oxide.

Table 1. Material properties of each oxide.

| Material Properties | Fe (Q345) | Fe ₂ O ₃ | Fe ₃ O ₄ |
|--|-----------|--------------------------------|--------------------------------|
| Density/ ρ (g/cm ³) | 7.86 | 5.24 | 5.18 |
| Specific heat capacity/ c (J/(Kg·K)) | 920 | 626 | 1350 |
| Thermal conductivity/ K (W/(cm·K)) | 0.52 | 0.04 | 0.02 |
| Melting temperature/ T_r (°C) | 1535 | 1565 | 1597 |
| Evaporation temperature / T_v (°C) | 2750 | 2700 | 3000 |
| Laser absorptivity/ A | 0.35 | 0.60 | 0.53 |

The layered geometric model for rust-oxide cleaning is shown in Figure 3, and several assumptions were ensured in the simulation.

- (1) The laser energy had Gaussian distribution on the material surface, and only the conduction of laser energy in the Z direction was considered.
- (2) The material surface was infinitely large, and the oxide layers and matrix were insulated on both sides.
- (3) L_1 , L_2 , and L_s represent the thickness of Fe₂O₃, Fe₃O₄, and matrix layers, respectively.
- (4) The Z-direction complied with the absorption law, and each parameter did not change with temperature.

Equations (1)–(6) describe one-dimensional heat-conduction formulas and boundary conditions [17,18].

$$\rho_i \cdot c_i \cdot \frac{\partial T(z, t)}{\partial t} = k_i \cdot \frac{\partial^2 T(z, t)}{\partial z^2}, \quad 0 \leq t \leq \tau \quad (1)$$

$$-k_1 \cdot \frac{\partial T_1(z, t)}{\partial z} \Big|_{z=0} = I_1 = A_1 \cdot I_0 \quad (2)$$

$$\frac{\partial T_s(z, t)}{\partial z} \Big|_{z=-L_1-L_2-L_s} = 0 \quad (3)$$

$$T_1(-L_1, t) = T_2(-L_1, t) \quad (4)$$

$$T_2(-L_1-L_2, t) = T_s(-L_1-L_2, t) \quad (5)$$

$$T(z, 0) = T_0 \quad (6)$$

where ρ is the density, c is the heat capacity, k is the thermal conductivity, A is the laser absorptivity, I is the peak power density, and T_0 is the environment temperature. A laser is applied to the material surface in heat flux, and its power distribution function is shown in Formula (7). The moving periodic pulse function comprises a Gaussian light source and regular operation. The repetition frequency was set to 10 kHz., and the laser pulse duration was 100 ns.

$$I = \begin{cases} A \cdot P \cdot (f \cdot \tau \cdot \pi r^2)^{-1} \cdot \exp\left(-2 \cdot \frac{(x-v_x t)^2 - y^2}{r^2}\right) & (N-1) \cdot t_p < t < (N-1) \cdot t_p + \tau \\ 0 & (N-1) \cdot t_p + \tau < t < N \cdot t_p \end{cases} \quad (7)$$

2.3. Design of Experiment and Analytical Methods

The laser's peak power density and scanning speed are the main factors that influence the temperature-field distribution of the material [19] and further influence the ablation depth of the surface oxide. This section designed a central composite test to optimize these two parameters with Comsol Multiphysics software. The experiment selected four cubic points, five center points of the cube, and four axis points and used Minitab software to generate 13 groups of tests automatically. Based on the peak power density and scanning speed commonly used in actual work, the experiment factor settings are shown in Table 2.

Table 2. Horizontal settings of experiment factors.

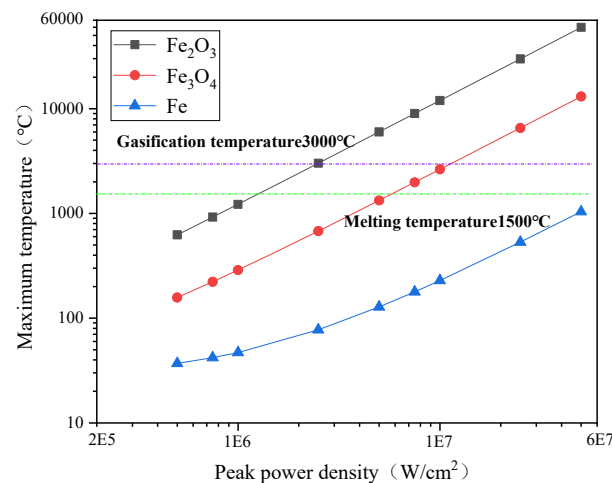
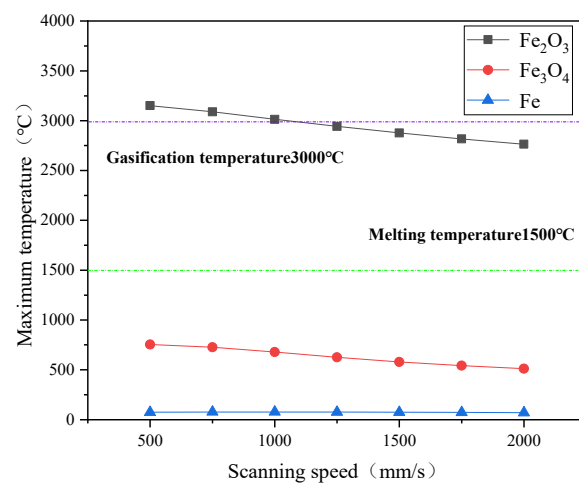
| The Serial Number | Name of Factor | Low Level | High Level |
|-------------------|---|-------------------|-------------------|
| 1 | Peak power density (W/cm^2) | 2.5×10^6 | 3.5×10^6 |
| 2 | Scanning speed (mm/s) | 1000 | 2000 |

To establish a quadratic single-removal volume-prediction model, Minitab software 6.0 was used to conduct a regression analysis, variance analysis, response surface, and isoline-map analysis on the test results. A white-light interferometer was used to measure the cleaning profile to verify the accuracy of the removal-volume model. In this study, the removal-volume prediction model of Fe_2O_3 (H1) and Fe_3O_4 (H2) was established to analyze the stepwise removal process based on layered corrosion oxides.

3. Experimental Results and Discussion

3.1. Distribution of Material Temperature Field

The maximum temperature of each material layer under different laser parameters in the simulation process is shown in Figures 4 and 5.

**Figure 4.** The relationship between the temperature of each layer material and the peak power.**Figure 5.** The relationship between the temperature of each layer of material and the scanning speed.

As seen from Figure 4, when the overlapping rate between adjacent spots was 50%, the maximum temperature of each layer of material gradually increased with the laser peak power density. For Fe_2O_3 , when the peak power density was $2.5 \times 10^6 \text{ W}/\text{cm}^2$, the maximum

surface temperature reached 3014.32 °C, which exceeded the evaporation temperature, and the material phase changed. The peak power density increased to 5×10^7 W/cm², and the maximum temperature of the surface reached 59,776.16 °C. The reason is that the thermal conductivity of the Fe₂O₃ layer is extremely low, laser-pulse energy acts at a nanosecond level, and the power accumulates on the surface in a short time, not transmitting and diffusing in time. Hence, the temperature rose to near 60,000 °C instantaneously.

The rust layer begins to melt and decompose when the maximum surface temperature exceeds its melting or evaporation temperature. For example, Fe₂O₃ will spoil and generate O₂ and Fe₃O₄. While gasifying, the decomposition product O₂ will also take away some oxides [20]. Therefore, when the maximum surface temperature of the material exceeds its melting or evaporation temperature, the subsequent temperature rise is of no real significance.

The size of the scanning speed is mainly reflected in the overlapping rate between adjacent spots. As seen in Figure 5, when the peak power density was fixed at 2.5×10^6 W/cm², the maximum temperature on the surface of each material decreased gradually. For Fe₂O₃, when the scanning speed was 500 mm/s, its maximum temperature was 3150.97 °C and the top temperature dropped to 2764.09 °C when the scanning speed increased to 2000 mm/s. This is because the overlapping rate between adjacent spots decreased with the addition of scanning speed.

In the cleaning process, the maximum temperature was small because the Fe₃O₄ and matrix were far away from the laser-acting area. It did not exceed its phase transition temperature, so the temperature rise had little effect.

3.2. Removal Test Results and Prediction Model

According to the simulation results, the ablation depth under each laser-cleaning parameter was obtained, as shown in Table 3. The corresponding simulation results of each parameter are shown in Figure 6.

Table 3. Ablation depth of the layered model under various laser parameters.

| Serial Number | Peak Power Density (W/cm ²) | Scanning Speed (mm/s) | Ablation Depth (μm) |
|---------------|---|-----------------------|---------------------|
| 1 | 2.5×10^6 | 2000.00 | 0.0 |
| 2 | 2.3×10^6 | 1500.00 | 0.0 |
| 3 | 2.5×10^6 | 1000.00 | 2.1 |
| 4 | 3.0×10^6 | 2207.11 | 4.1 |
| 5 | 3.0×10^6 | 1500.00 | 7.8 |
| 6 | 3.0×10^6 | 792.89 | 17.5 |
| 7 | 3.5×10^6 | 2000.00 | 12.9 |
| 8 | 3.7×10^6 | 1500.00 | 20.9 |
| 9 | 3.5×10^6 | 1000.00 | 28.5 |

3.2.1. Regression Analysis and Variance Analysis

Based on the center composite test design, the effects of laser peak power density and scanning speed on ablation depth were investigated and the corresponding quadratic regression model was built. The regression coefficients estimated by coding units in the quadratic regression model are shown in Table 4.

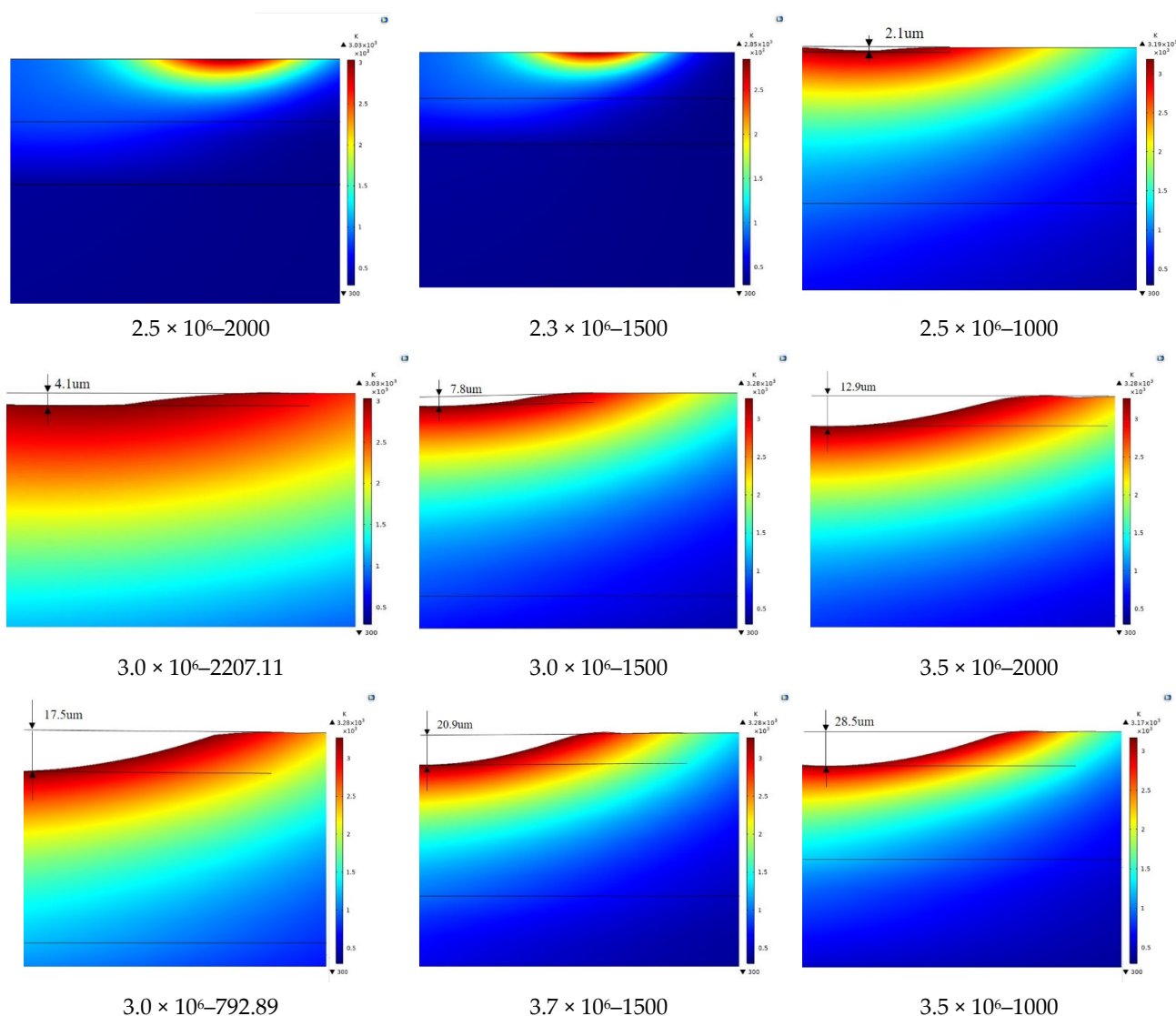


Figure 6. Ablation depth under different laser parameters.

Table 4. Estimated regression coefficient of ablation depth.

| Item | Coefficient | Coefficient Standard Error | T | P |
|-----------------------|-------------|----------------------------|-------|-------|
| Constant | 7.800 | 0.590 | 13.22 | 0.000 |
| Peak power density I | 8.607 | 0.466 | 18.45 | 0.000 |
| Scanning speed v | −4.581 | 0.466 | −9.82 | 0.000 |
| Peak power density I* | 1.388 | 0.500 | 2.77 | 0.028 |
| Scanning speed v* | 1.563 | 0.500 | 3.12 | 0.017 |
| Scanning speed v | −3.375 | 0.660 | −5.12 | 0.001 |

Table 4 shows that the *p*-values were all less than 0.05, corresponding to the primary and secondary main effects, so their influence was significant.

According to the variance analysis in Table 5, the two determination coefficients, R-sq and R-sq (Adjustment), were 98.56% and 97.53%, respectively. The gap between them was small, close to 1, showing a high regression, indicating that the established ablation depth model was good and the regression equation was not misfitted.

Table 5. Variance analysis of ablation depth. R-sq = 98.56% R-sq (adjustment) = 97.53% R-sq (prediction) = 89.75%.

| Source | Degrees of Freedom | Adj SS | Adj MS | F | P |
|------------------------|--------------------|---------|---------|--------|-------|
| Model | 5 | 833.031 | 166.606 | 95.70 | 0.000 |
| Linear | 2 | 760.569 | 380.284 | 218.45 | 0.000 |
| Peak power density I | 1 | 592.662 | 592.662 | 340.44 | 0.000 |
| Scanning speed v | 1 | 167.907 | 167.907 | 96.45 | 0.000 |
| Square | 2 | 26.899 | 13.450 | 7.73 | 0.017 |
| Peak power density I* | 1 | 13.392 | 13.392 | 7.69 | 0.028 |
| Peak power density I | 1 | 13.392 | 13.392 | 7.69 | 0.028 |
| Scanning speed v* | 1 | 16.984 | 16.984 | 9.76 | 0.017 |
| Scanning speed v | 1 | 16.984 | 16.984 | 9.76 | 0.017 |
| Two-factor interaction | 1 | 45.562 | 45.562 | 26.17 | 0.001 |
| Peak power density I* | 1 | 45.562 | 45.562 | 26.17 | 0.001 |
| Scanning speed v | 1 | 45.562 | 45.562 | 26.17 | 0.001 |
| Error | 7 | 12.186 | 1.741 | | |
| Loss of quasi | 3 | 12.186 | 4.062 | * | * |
| Pure error | 4 | 0.000 | 0.000 | | |
| Total | 12 | 845.217 | | | |

“*” in Source stands for multiplication.

The “*” of the F value indicates that the F value reaches 0.05 level significant, that is, the F value reaches significant. *p* value is an indicator to measure the difference between the control group and the experimental group. “*” means that *p* value is less than 0.05, indicating that there is a significant difference between the two groups.

3.2.2. Prediction Model of Removal Volume

The quadratic-regression equation of Fe₂O₃-layer ablation depth can be obtained through regression analysis and variance analysis, namely, the single-removal quantity-prediction model.

$$H_1 = -26.8 + 4.2 * 10^6 * I + 1.259 * 10^2 * v + 5.55 * 10^{12} * I^2 + 6 * 10^6 * v^2 - 1.350 * 10^8 * I * v + \zeta \quad (8)$$

where H₁ is the ablation depth of the Fe₂O₃ layer, I is the laser peak power density, v is the scanning speed, and ζ is the error. As for the Fe₃O₄ layer, its properties differ from those of the Fe₂O₃ layer. In addition, based on the central composite test design, the prediction model of the single removal quantity obtained is shown as Formula 2.

$$H_2 = -13.2 + 1.29 * 10^6 * I + 7.44 * 10^3 * v + 3.0 * 10^{12} * I^2 + 3 * 10^6 * v^2 - 7.1 * 10^9 * I * v + \zeta \quad (9)$$

where H₂ is the ablation depth of the Fe₃O₄ layer, I is the laser peak power density, v is the scanning speed, and ζ is the error.

3.3. Analysis of Stepwise Removal Process for Layered Rust Oxides

According to the composition of the oxide layer, the actual laser-cleaning process can be divided into three stages: (I) Cleaning the Fe₂O₃ layer, (II) cleaning the Fe₂O₃ and Fe₃O₄ layers simultaneously, and (III) cleaning Fe₃O₄ layer. The single removal volume of stage 1 and stage 3 follow Formulas 8 and 9, respectively. When laser cleaning is used to clean two layers of materials simultaneously, it is assumed that the total absorbed energy is E, and the energy absorbed by Fe₂O₃ is E₁. The energy absorbed by Fe₃O₄ is E₂, then the single-removal volume-prediction model is H₃, as shown in Formula 10.

$$H_3 = \alpha * H_1 + \beta * H_2 = \frac{E_1}{E} * H_1 + \frac{E_2}{E} * H_2 = \frac{E_1}{E_1 + E_2} * H_1 + \frac{E_2}{E_1 + E_2} * H_2 \quad (10)$$

Figure 7 shows the flow chart of laser cleaning for rust-layered oxides. I_{max} , v^* , L_1 , and L_2 input values represent the initial peak power density, initial scanning speed, and thickness of the Fe_2O_3 layer and Fe_3O_4 layer, respectively. h_i represents the total removal volume of laser cleaning. Δh represents the single removal volume of each stage. I^* represents the peak power density adjusted during the last cleaning. The initial values of I , h_0 , and Δh were 0.

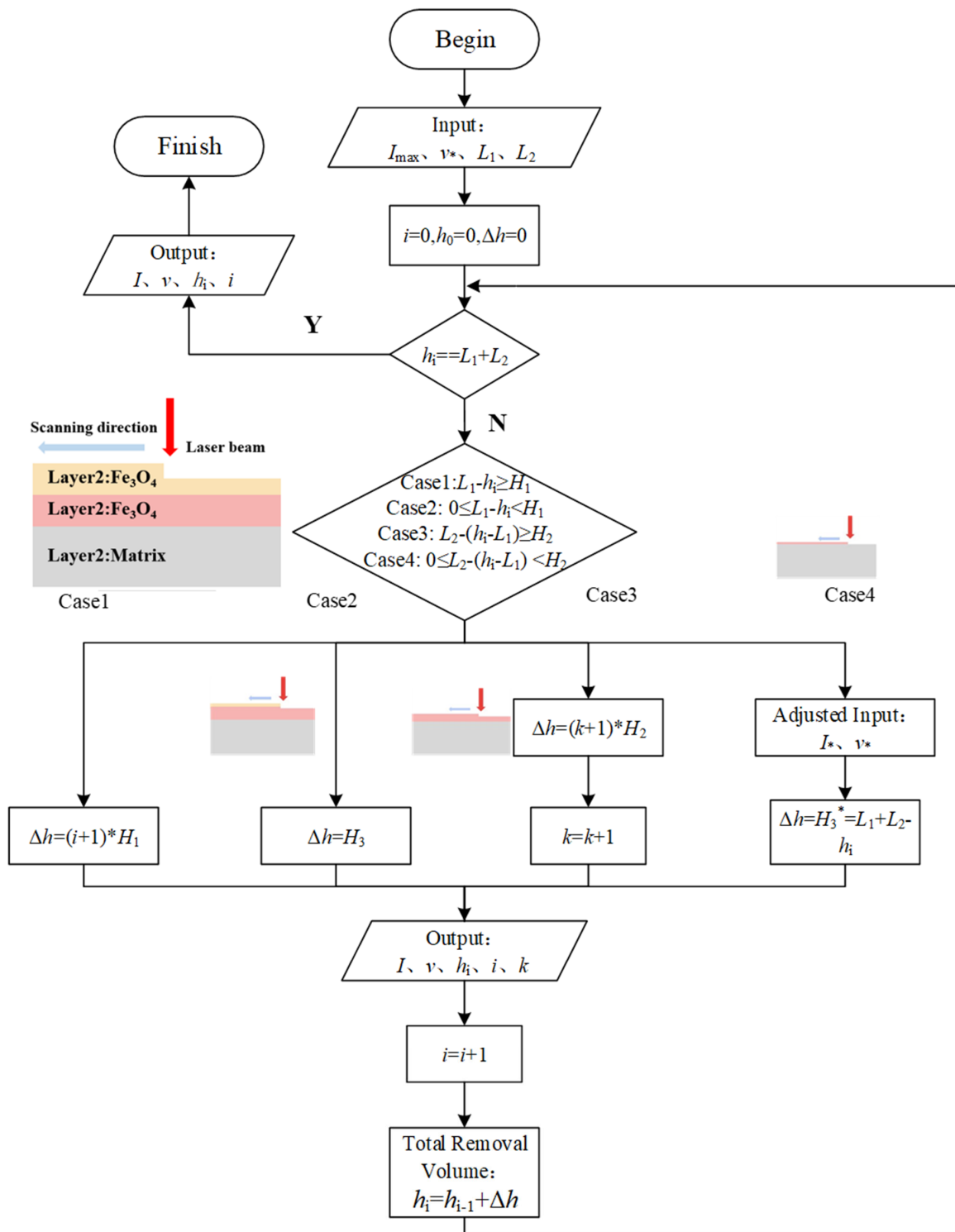


Figure 7. Flow chart of laser cleaning for layered rust oxides.

Based on the thickness L_1 and L_2 of the Fe_2O_3 and Fe_3O_4 layers, the initial peak power density I_{max} and scanning speed v^* were input. Firstly, the relationship between the total removal volume and the total thickness of the oxide layers was determined. When the total removal volume was less than the thickness of the oxide layer, the cleaning process was selected according to other judgment conditions. Case 1: When the residual thickness of Fe_2O_3 was more significant than its single removal volume H_1 , the removal process was stage (I) and Formula (8) was calculated. Case 2: When the residual thickness of Fe_2O_3 was less than its single removal volume H_1 , the removal process was stage II and Formula (10) was calculated. Case 3: When the residual thickness of Fe_3O_4 was more significant than its single removal volume H_2 after the Fe_2O_3 layer was obliterated, the removal process was stage III and Formula (9) was calculated. Case 4: When the residual thickness of Fe_3O_4 was less than its single removal volume H_2 , the initial peak power density needed to be adjusted from I_{max} to I^* according to Formula (9) so that the single removal amount under the initial peak power density and scanning speed was H_3^* , that is, to ensure the oxide layer on the matrix surface was entirely removed the last time. The corresponding peak power density I , scanning speed v , cleaning depth h_i , and cleaning times i were output in each run of Case 1 to Case 4. The operation was stopped when the oxide layer was removed, and final cleaning parameters and cleaning times were output.

4. Verification

To verify the accuracy of the prediction model, three different parameters were selected to conduct a single cleaning experiment for each layer (Fe_2O_3 , Fe_3O_4) of materials. Carbon steel with a size of $20 \text{ mm} \times 20 \text{ mm}$ was selected as the sample. The sample morphology after cleaning is shown in Figure 8. The white-light interferometer was used to measure the contour of the cleaning groove, and the polynomial was used for fitting, as shown in Figure 9.

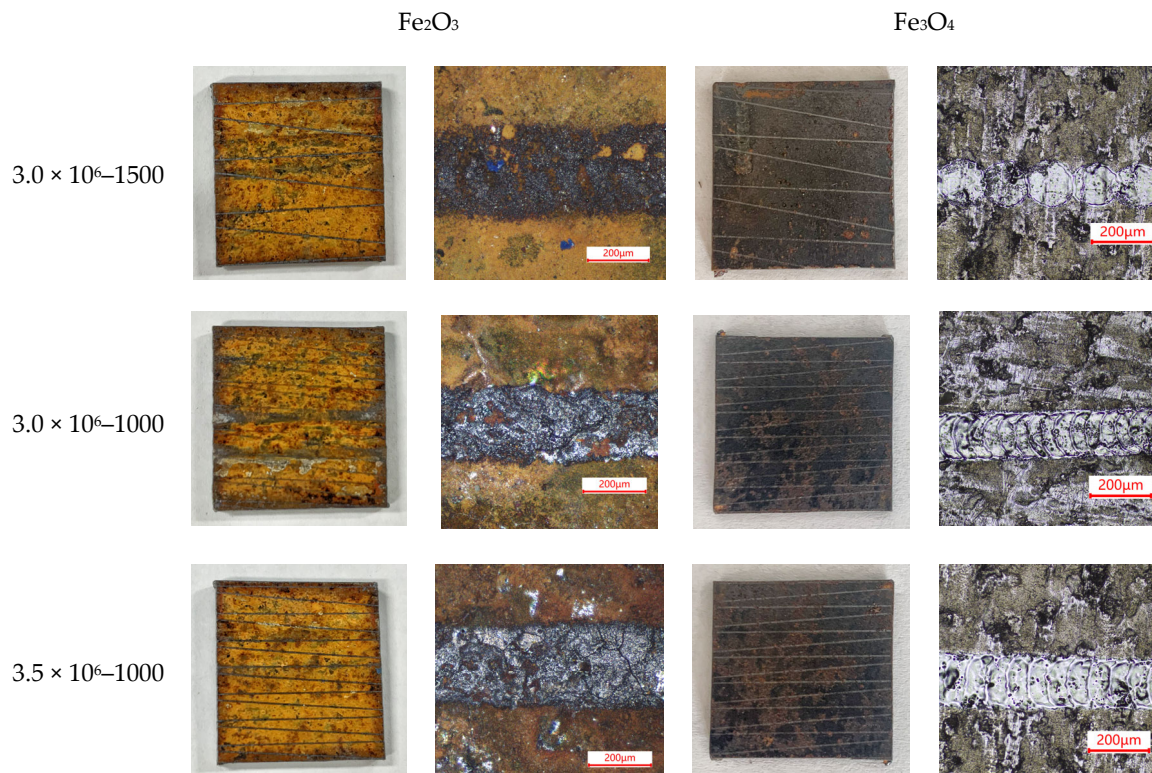


Figure 8. The surface morphology of each layer was cleaned by a single laser time.

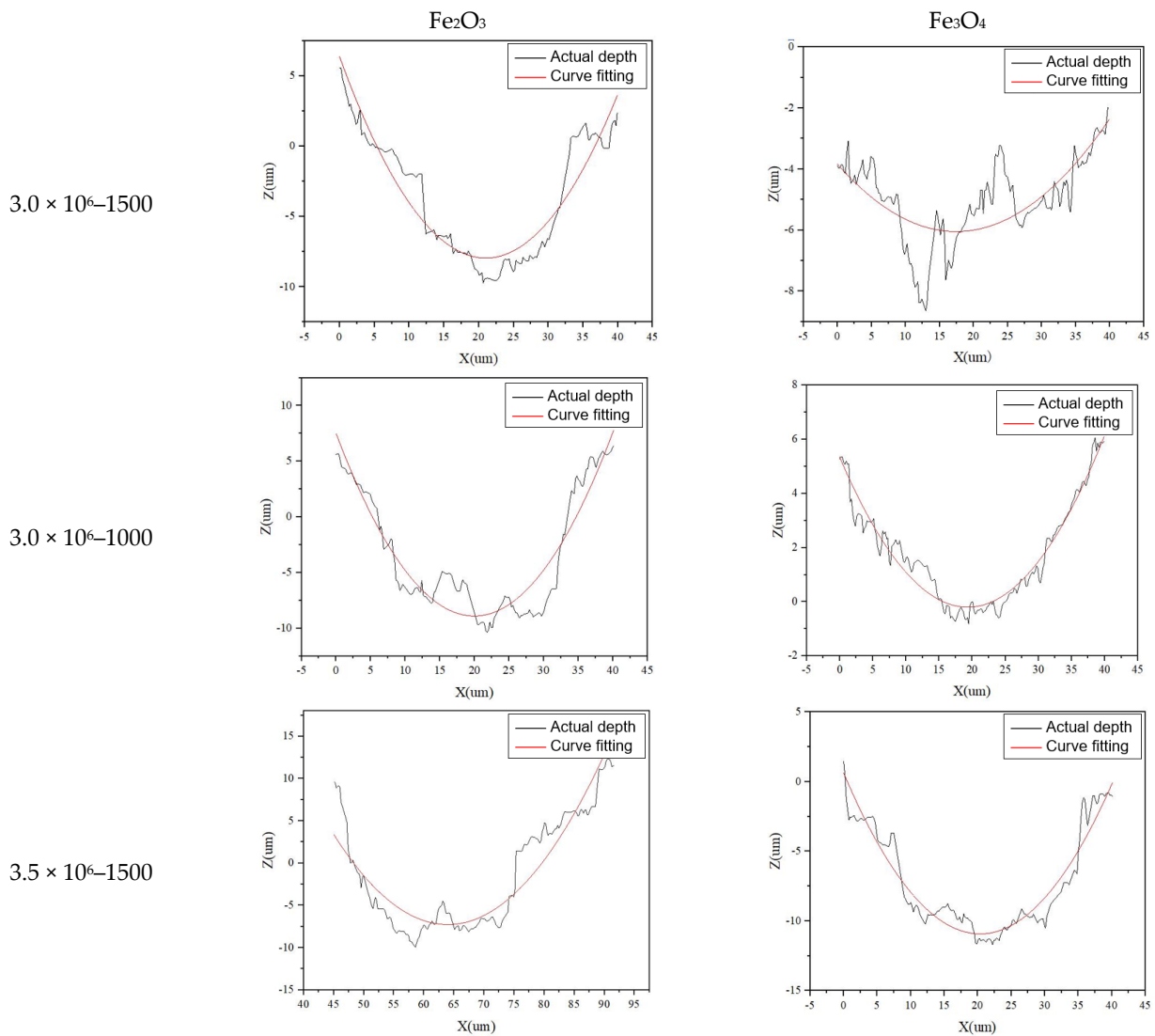


Figure 9. The groove contour after cleaning under different parameters.

The actual measured and theoretically calculated values were compared and analyzed, as shown in Table 6. As can be seen from Table 6, there was a specific difference between the measured value and the theoretical value. However, with the increased ablation depth, the measured value was closer to the theoretical value. All the errors between the test results and the theoretical calculation values were within a reasonable range, proving that the established single-removal volume-prediction model of rusty oxide was effective.

Table 6. Comparative analysis of measurements and under different parameters.

| Parameters | $3.0 \times 10^6-1500$ | | $3.0 \times 10^6-1000$ | | $3.5 \times 10^6-1500$ | |
|------------|-------------------------|-------------------------|-------------------------|-------------------------|-------------------------|-------------------------|
| Layers | Fe_2O_3 | Fe_3O_4 | Fe_2O_3 | Fe_3O_4 | Fe_2O_3 | Fe_3O_4 |
| M-value | 8.400 | 2.900 | 14.200 | 6.300 | 17.500 | 9.400 |
| T-value | 7.385 | 3.630 | 13.840 | 6.810 | 17.398 | 8.700 |
| Error | 13.744% | 20.110% | 2.601% | 7.489% | 0.586% | 8.046% |

Based on the established prediction model of single removal volume and the cleaning flow chart of the layered rust model, the actual mining samples were cleaned by laser for verification. The morphology of the selected sample and the thickness of the dirt layer are shown in Figure 10. Firstly, parameters with a peak power density of $3.5 \times 10^6 \text{ W/cm}^2$ and

scanning speed of 1000 mm/s were used for cleaning twice. After cleaning, the surface morphology and remaining thickness of dirt were determined, as shown in Figure 11. The residual dirt was only Fe_3O_4 , and the thickness of the dirt layer was only 20 μm . The laser parameters were adjusted to the peak power density of $3.7 \times 10^6 \text{ W}/\text{cm}^2$ and the scanning speed to 1500 mm/s according to the single-removal volume-prediction model. In this process, the single removal volume was 10.5 μm , so the remaining oxide layer could be removed entirely after cleaning twice.

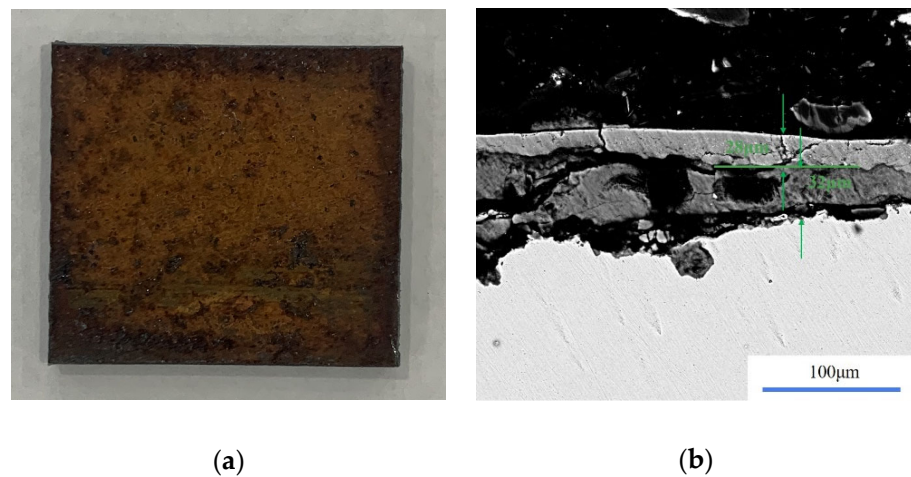


Figure 10. Morphology of sample to be cleaned and thickness of oxide layer. (a) Morphology of sample to be cleaned; (b) thickness of oxide layer.

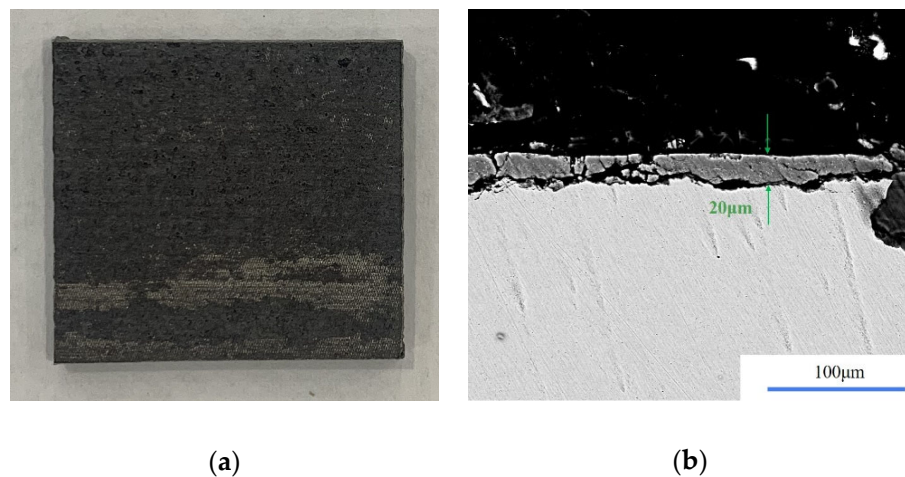


Figure 11. Morphology and thickness of residual dirt after cleaning twice. (a) Morphology of sample after cleaning; (b) thickness of residual oxide.

Based on adjusted laser parameters, the surface morphology of the Fe_3O_4 layer after cleaning twice was determined, as shown in Figure 12. It can be seen that the sample surface began to expose the metal matrix, and only a small amount of particulate matter remained on the metal surface, which showed a good cleaning effect. According to the above experimental results, it was proven that the flow chart of laser cleaning layered rust oxides can be used to guide actual cleaning work.

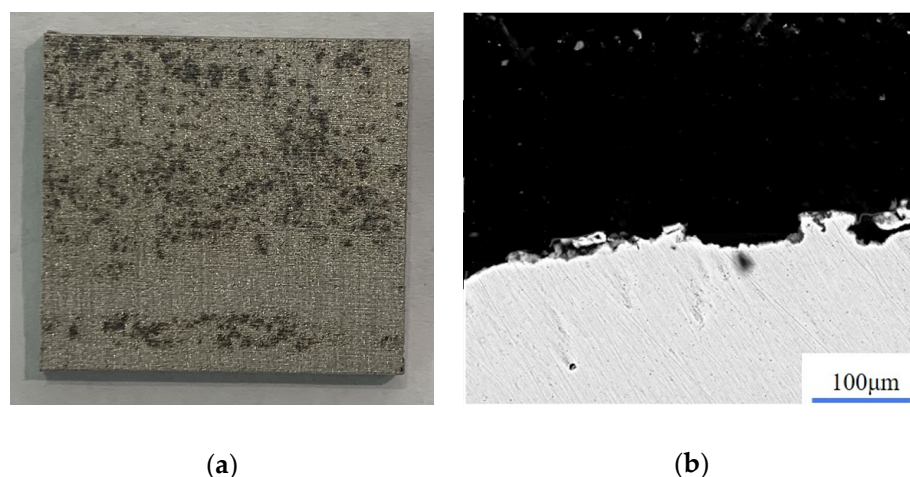


Figure 12. Surface morphology after complete cleaning. (a) Morphology of sample after cleaning twice; (b) thickness of residual oxide.

5. Conclusions

In this paper, based on the properties of the rusty oxide, the prediction model for a single removal volume of oxides was established, which can guide the efficient and precise cleaning of the oxide without damaging the surface of the substrate. The main conclusions can be listed as follows:

- (1) The main dirt on the surface of engineering machinery was layered oxide, the composition of the surface layer was Fe_2O_3 , and the design of the bottom surface layer was Fe_3O_4 .
- (2) A central composite test of peak power density and scanning speed was designed with the help of Comsol Multiphysics software. In this process, the prediction model test of single removal volume for different oxides was established, and experiments proved the model.
- (3) Based on the response surface and contour map, when the laser energy exceeded the material cleaning threshold, the ablation depth of oxide increased with the peak power density and the decrease in scanning speed.
- (4) Based on the established prediction model of single removal volume, the stepwise removal process of rust-layered oxides was analyzed. The oxide composition to be cleaned was divided into three stages: (I) cleaning the Fe_2O_3 layer, (II) cleaning the Fe_2O_3 and Fe_3O_4 layers simultaneously, and (III) cleaning Fe_3O_4 layer.

Author Contributions: Conceptualization, Y.R. and X.M.; methodology, M.M. and L.W.; validation, J.L. and W.C.; formal analysis, M.M. and X.M. and Y.L.; investigation, Y.R.; data curation, Y.R. and B.L.; writing—original draft preparation, Y.R.; essay—review and editing, L.W.; project administration, J.L. All authors have read and agreed to the published version of the manuscript.

Funding: This research was supported by the National Natural Science Foundation of China (grant No. 52175473). The Province Key R&D Program of Shandong (grant No. 2020JMRH0504). Jinan “20 New Universities” Funding Project (2021GXRC066).

Institutional Review Board Statement: The study was conducted by the Declaration of Helsinki and approved by the Institutional Review Board of Shandong University.

Informed Consent Statement: Informed consent was obtained from all subjects involved in the study.

Conflicts of Interest: The authors declare no conflict of interest.

References

1. Fauchais, P. Understanding plasma spraying. *J. Phys. D Appl. Phys.* **2004**, *37*, R86–R108. [[CrossRef](#)]
2. Naskoudakis, I.; Petroutsatou, K. A Thematic Review of Main Researches on Construction Equipment Over the Recent Years. *Procedia Eng.* **2016**, *164*, 206–213. [[CrossRef](#)]

3. Jeon, H.W.; Jung, I.S.; Lee, C.S. Risk Assessment for Reducing Safety Accidents caused by Construction Machinery. *J. Korean Soc. Saf.* **2013**, *28*, 64–72. [[CrossRef](#)]
4. Zhou, Z.; Ruan, D.N.; Jiang, L.M. Comparison on treatment strategy for chemical cleaning wastewater: Pollutants removal, process design, and techno-economic analysis. *J. Environ. Manag.* **2019**, *235*, 161–168. [[CrossRef](#)] [[PubMed](#)]
5. Grigoras, C.C.; Chirita, B. The analysis of high-pressure water jet cutting of thick aluminum alloy 6061-T651 from a statistical perspective. *Mater. Sci. Eng.* **2020**, *916*, 012043–012049.
6. Choi, J.P.; Lee, S.J. Efficient Chip Breaker Design by Predicting the Chip Breaking Performance. *Int. J. Adv. Manuf. Technol.* **2001**, *17*, 489–497. [[CrossRef](#)]
7. Watkins, K.G. Mechanisms of laser cleaning. *Adv. High-Power Lasers Appl.* **2000**, *3888*, 165–174.
8. Hu, C.Y.; He, G.Y.; Chen, J. Research on Cleaning Mechanism of Anti-Erosion Coating Based on Thermal and Force Effects of Laser Shock. *Coatings* **2020**, *10*, 683. [[CrossRef](#)]
9. Ristic, S.; Polic, S. Laser cleaning textile artifacts with metal threads: Process parameter optimization. *Sci. Tech. Rev.* **2014**, *64*, 45–52.
10. Osticioli, I.; Siano, S. Dependence of Nd: YAG laser derusting and passivation of iron artifacts on pulse duration. In Proceedings of the Conference on Fundamentals of Laser-Assisted Micro- and Nanotechnologies, St. Petersburg, Russian, 24–28 June 2013; Volume 9065, p. 906513.
11. Ali, S.N.; Taha, Z.A.; Mansour, T.S. Laser Cleaning Using Q-Switched Nd: YAG Laser of Low Carbon Steel Alloys. *Adv. Condens. Matter Phys.* **2014**, *2014*, 418142. [[CrossRef](#)]
12. Xu, J.W.; Wu, C.W.; Zhang, X. Influence of parameters of a laser cleaning soil rust layer on the surface of ceramic artifacts. *Appl. Opt.* **2019**, *58*, 2725–2730. [[CrossRef](#)] [[PubMed](#)]
13. Yue, L.Y.; Wang, Z.B.; Li, L. Modeling and simulation of laser cleaning of tapered micro-slots with different temporal pulses. *Opt. Laser Technol.* **2013**, *45*, 533–539. [[CrossRef](#)]
14. Lu, Y.; Yang, L.J.; Wang, M.L. Simulation of nanosecond laser cleaning the paint based on the thermal stress. *Optik-International J. Light Electron Opt.* **2021**, *227*, 165589. [[CrossRef](#)]
15. Marimuthu, S.; Mhich, A.; Ahmed, A.; Molchan, I.S. Numerical Simulation of Excimer Laser Cleaning of Film and Particle Contaminants. *J. Heat Transf.* **2013**, *135*, 121301. [[CrossRef](#)]
16. Piekarska, W.; Kubiak, M. Theoretical investigations into heat transfer in laser-welded steel sheets. *J. Therm. Anal. Calorim.* **2012**, *110*, 159–166. [[CrossRef](#)]
17. Zou, W.F.; Xie, Y.M.; Xiao, X. Application of thermal stress model to paint removal by Q-switched Nd: YAG laser. *Chin. Phys. B* **2014**, *23*, 433–438. [[CrossRef](#)]
18. Zhang, G.X.; Hua, X.M.; Huang, Y.; Zhang, Y.L. Investigation on mechanism of oxide removal and plasma behavior during laser cleaning on aluminum alloy. *Appl. Surf. Sci.* **2020**, *506*, 144666. [[CrossRef](#)]
19. Wang, Z.M.; Zeng, X.Y.; Huang, W.L. Parameters and surface performance of laser removal of rust layer on A3 steel. *Surf. Coat. Technol.* **2003**, *166*, 10–16. [[CrossRef](#)]
20. Zeng, X.D.; Qin, W.B.; Li, J. Research on mechanism and process of paint removal with pulsed fiber laser. *MATEC Web Conf.* **2018**, *189*, 01008–01015. [[CrossRef](#)]